JOURNAL OF PROPULSION AND POWER
Vol. 21, No. 3, May–June 2005

Mechanistic Model for Aluminum Particle Ignition and Combustion in Air

Paul E. DesJardin,* James D. Felske,† and Mark D. Carrara‡
State University of New York at Buffalo, Buffalo, New York 14260-4400

A mechanistic model for the ignition and combustion of an isolated aluminum particle burning in air is presented. The model consists of two stages, ignition and combustion. In the ignition stage, melting and heterogeneous surface reactions (HSR) are assumed to occur until a predefined transition temperature of the oxide is attained. In the combustion stage, a quasi-steady state diffusion flame is assumed, and a new conserved scalar formulation is presented that accounts for the deposition of metal oxide on the surface of the molten aluminum. A system of nonlinear ordinary differential equations that describes each stage self-consistently with the gas-phase analysis is developed. Representative results are presented for a range of ambient temperature conditions and compared to experimental measurements. Predictions of overall burn rates, particle velocity, and flame radius show good agreement with experimental data. Also discussed is the extension of the conserved scalar approach to include a more generalized oxidizing environment as well as HSR from nitride reactions during the quasi-steady burning stage.

Nomenclature

A	=	surface area
A_1	=	preexponential constant
B	=	transfer number
Bi	=	Biot number
C	=	specific heat
C_D	=	drag coefficient
D	=	diameter
D_{l+s}	=	particle diameter from liquid and solid phases
D_m	=	diffusivity coefficient
E_a	=	activation energy
f	=	ratio of metal-oxide surface sink to total mass flux
h	=	convection coefficient, total enthalpy (i.e., sensible plus chemical)
h_{lg}	=	heat of vaporization
$h_{\mathrm{r,gs}}$	=	heat of reaction for homogeneous gas-phase reactions
$h_{\mathrm{r,ls}}$	=	heat of reaction for heterogeneous surface reactions
k	=	thermal conductivity
m	=	mass
$\dot{m}_{\mathrm{lg}}$	=	mass evaporation rate of liquid aluminum from evaporation
$\dot{m}_{\mathrm{ls}}$	=	mass consumption rate of liquid aluminum to form solid aluminum oxide (Al_2O_3)
$\dot{m}_{\mathrm{sl}}$	=	mass transfer rate from solid to a liquid during melting
Nu	=	Nusselt number
P	=	pressure
Pr	=	Prandtl number
$\dot{Q}_{\mathrm{conv}}$	=	energy source/sink term from convection
$\dot{Q}_{\mathrm{HSR}}$	=	energy source term from heterogeneous combustion
$\dot{Q}_{\mathrm{melt}}$	=	energy sink term from melting
$\dot{q}''_c$	=	heat-conduction flux
$\dot{q}''_{\mathrm{rad}}$	=	radiative heat flux
$\mathcal{R}$	=	universal gas constant
Re	=	Reynolds number
Sc	=	Schmidt number
Sh	=	Sherwood number
T	=	temperature
T_b	=	boiling temperature
T_M	=	melting temperature
T_{trans}	=	transition temperature
t	=	time
$\boldsymbol{u}$	=	velocity
Y_{ox}	=	mass fraction
α	=	ratio of the particle liquid mass to liquid plus solid mass, i.e., $\alpha = m_l/(m_l + m_s)$
μ	=	molecular viscosity
ν_i	=	stoichiometric ratio of mass of ith species consumed/produced per unit mass of metal (Note, the sign convention chosen is $\nu_i > 0$ for consumption and $\nu_i < 0$ for production for convenience in defining the coupling functions.)
ρ	=	density

Subscripts

g	=	gas property
l	=	liquid metal property
m	=	vapor metal property
mox	=	metal-oxide property
ox	=	oxidizer property
P	=	mass weighted particle property
p	=	product gas property
s	=	solid metal property
slg	=	surface property at liquid–gas interface
sls	=	surface property at liquid–solid interface
T	=	mixture weighted property for gas and metal-oxide particles
∞	=	far-field gas-phase property

Received 16 October 2003; revision received 31 August 2004; accepted for publication 20 October 2004.

*Assistant Professor, Department of Mechanical and Aerospace Engineering; ped3@eng.buffalo.edu.

†Professor, Department of Mechanical and Aerospace Engineering.

‡Research Assistant, Department of Mechanical and Aerospace Engineering.

I. Introduction

EXTENSIVE research on the burning of aluminum particles has been conducted since the early 1960s. Aluminum powder additives have found use in applications ranging from enhancing the specific thrust for propellants in rocket motors to the formulation of advanced energetic materials for the design of explosives. A summary of the present understanding of aluminum combustion can be found in the review by Williams.[1]

The ignition of aluminum particles begins with a relatively short heterogeneous combustion stage and quickly transitions to a quasi-steady diffusion flame with a detached spherical flame

positioned off the particle surface at two to five radii.[2,3] In addition to gaseous products from the flame, solid oxide condensates accumulate on the leeward side of the particle, forming a cap. This cap reduces the overall surface area of the aluminum and in some cases results in violent surface gas ejections caused by both the dilution of molten aluminum with oxides and the participation of nitride reactions.[4–6] These events are especially severe in water vapor environments and result in particle cracking and fragmentation.[6]

Early semi-analytical theoretical models of aluminum combustion have focused on the quasi-steady burning stages.[7–9] These models employ flame sheet approximations and decompose the transport of heat and mass into two zones: a region between the particle surface and the flame and a region beyond the flame. Results using these models have been shown to provide reasonable predictions for burning rates for a variety of oxidizing environments.[9,10] Liang and Beckstead and Widener et al. investigated a more detailed description of the flame and flow around the particle but found that many of the aspects of the flame structure and overall burning rates are close to that obtained using flame sheet assumptions.[11,12] Most recently, Babuk and Vasilyev have devised a five zone model that includes a more complete description of oxide cap formation, growth and movement.[13] They demonstrate that their model is capable of capturing many of the observed dynamics of agglomerate motion. In all of these previous studies, only the late time combustion regime of the particle had been considered.

The focus of the present research is on the development of a relatively simple mechanistic model to account for both the early ignition and the late time quasi-steady burning modes of aluminum particles which include heating, melting, heterogeneous surface reactions (HSR), gas-phase combustion, and metal-oxide cap formulation. In addition, a new conserved scalar formulation is presented for the quasi-steady burning stage, which includes the effects of metal-oxide deposition on the particle surface. This new approach allows for the relaxation of flame sheet assumptions that have been largely used in previous developments.[8,10] It is highly desirable for the mechanistic model to be computationally efficient because it will later be used as a submodel in larger scale numerical simulations of highly energetic, multiphase, turbulent flows. Approximations are therefore introduced to capture only the leading-order effects of particle ignition and combustion on the surrounding temperature environment, that is, a lumped model, constant thermal properties, etc.

The remainder of this study begins with the mathematical formulation of the model and extensions to include a more generalized oxidizing environment and nitride HSR. Results are then presented with comparison to experimental data. Finally, conclusions are drawn and a summary of findings is presented.

II. Model Formulation

The particle is assumed to be spherically symmetric and treated using a lumped capacitance approach because the Biot number Bi $(=h_P D_P/k_P)$ is estimated to be no larger than 0.01 for all cases considered. The ignition and combustion of the aluminum particle is modeled in two stages. In the first stage, stage I, the particle undergoes rapid heating followed by melting from convection heat transfer. HSR are taken into account (see Fig. 1) and result in additional heating of the particle until a transition temperature T_{trans} is attained. Previous studies have suggested that the transition from stage I to quasi-steady burning (stage II) corresponds to the melting temperature of the metal oxide. As will be discussed in the results, the exact value of transition temperature turns out to not be that important within the approximations that will be used to model ignition. In the second stage, the oxide layer skin surrounding the particle is assumed to peel back and coalesce into a cap on the downstream side of the particle (see Fig. 2). Molten metal is exposed to the surrounding gas, and a detached diffusion flame is established at two to five particle radii.

A. Stage I—Ignition

Prediction of the early time ignition characteristics of aluminum is extremely challenging. Previous studies of aluminum oxidation, which had the goal of understanding high-temperature corrosion phenomena, have highlighted the complexity of predicting oxide growth. This complexity includes the effects of ion and electron transport in the oxide shell and associated formation of internal electric fields, diffusion of oxidizer along grain boundaries, macroscopic diffusion effects from oxide fracture, and the importance of accounting for metal impurities.[14–17] Needless to say, a complete description of aluminum-oxide growth is still not within reach, and pursuing this goal is outside the scope of the present work. Alternatively, a phenomenological description of the ignition characteristics is desirable. Several Arrhenius-based models have been postulated.[18–20] Several models are summarized in Ref. 21. The Arrhenius preexponential and activation energy factors for the current study are taken from the work of Servaites et al., Foelsche et al., Roberts et al., which are empirically determined from experiments in which aluminum particles are exposed to shock ignited O_2, $H_2O/O_2/Ar$ and $CO_2/O_2/Ar$ environments.[20,22,23] The reason for this selection is that the conditions of their experiment best match the intended use of the current model for larger scale simulations of shock dispersal events.

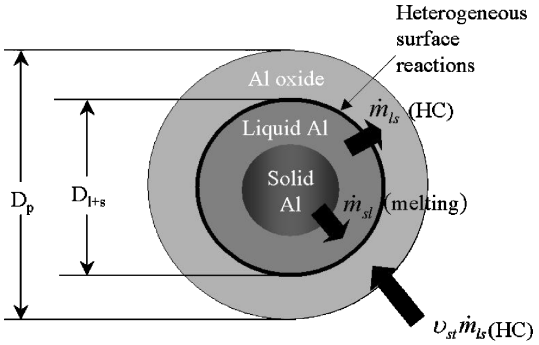

Fig. 1 Sketch of stage I heterogeneous particle ignition. Note, the thickness of the oxide layer is exaggerated for clarity.

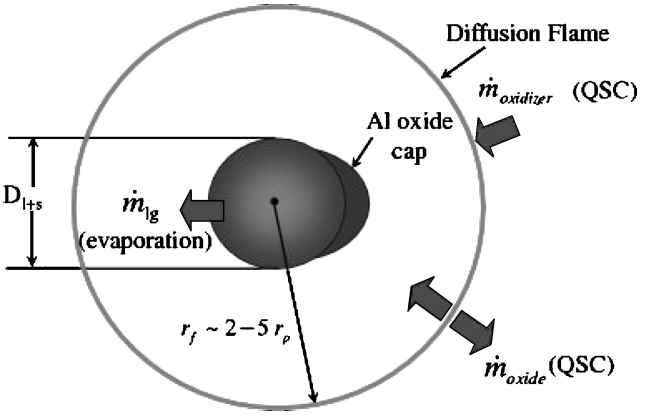

Fig. 2 Sketch of stage II flame sheet particle combustion.

Figure 1 shows the relatively simple description of particle ignition consisting of solid metal m_s and liquid metal m_l surrounded by a layer of metal oxide m_{mox}. Upon heating, the particle temperature increases until a melting phase transition occurs. Melting is monitored with a progress variable α, defined as the mass fraction of liquid in the particle, $\alpha = m_l/(m_l + m_s)$. If $\alpha > 0$, then metal oxide is assumed to form at the liquid/metal-oxide interface as result of oxygen having diffused through the metal-oxide shell through its grain boundaries. Other diffusion mechanisms might also be present, but these mechanisms are thought to be of secondary importance in comparison to grain boundary diffusion and therefore are neglected.[14,15] Based on a control volume analysis surrounding the oxide shell, a set of nonlinear ordinary differential equations describing mass, momentum, and energy conservation are derived

and given by

$$\frac{d\alpha}{dt} = \frac{1}{m_l + m_s}[\dot{m}_{sl} - (1-\alpha)\dot{m}_{ls}] \quad (1)$$

$$\frac{dm_l}{dt} = \dot{m}_{sl} - \dot{m}_{ls} \quad (2)$$

$$\frac{dm_P}{dt} = \nu_{ox}\dot{m}_{ls} \quad (3)$$

$$m_P\frac{d\boldsymbol{u}_P}{dt} = \frac{\pi}{8}\rho_g D_P^2 C_D|\boldsymbol{u}_g - \boldsymbol{u}_P|(\boldsymbol{u}_g - \boldsymbol{u}_P) + m_P\boldsymbol{g} \quad (4)$$

$$\begin{aligned} m_P C_P\frac{dT_P}{dt} &= \dot{Q}_{conv} + \dot{Q}_{rad} - \dot{Q}_{melt} + \dot{Q}_{HSR} \\ &= \pi D_P\frac{\mu_g C_g}{Pr_g}(T_g - T_P)Nu_P \\ &\quad - \dot{q}''_{rad}A_P - h_{ls}\dot{m}_{sl} - \dot{m}_{ls}h_{r,ls} \end{aligned} \quad (5)$$

Equations (1) and (2) describe the time rate of change of liquid mass fraction and overall liquid mass in the droplet. These equations have source and sink terms associated with aluminum melting $\dot{m}_{sl}$ and HSR $\dot{m}_{ls}$, respectively (see Fig. 1), and are determined from the following relations:

$$\dot{m}_{sl} = \begin{cases} (\dot{Q}_{conv} + \dot{Q}_{HSR})/h_{ls} & \text{for} \quad 0 < \alpha < 1 \quad \text{and} \quad T_P = T_{M,Al} \\ 0 & \text{otherwise} \end{cases}$$

$$\dot{m}_{ls} = \begin{cases} A_{sls}A_1\exp(-E_a/\mathcal{R}T_{sls}) & \text{for} \quad \alpha > 0 \\ 0 & \text{otherwise} \end{cases}$$

where the values of the preexponential coefficient A_1 and activation energy E_a are given in Table 1 from the study of Roberts et al.[23] It should be emphasized that A_1 and E_a are, in general, functions of the surrounding gas pressure and oxidizing environments, and therefore the values used here are only applicable for HSR in O_2 environments. The material consumed from HSR is assumed to be small so that the surface area of the heterogeneous reaction front A_{sls} is set equal to the surface area of the particle A_P. It is assumed that the temperature at the reaction surface T_{sls} is the same as the temperatures of the liquid and solid aluminum T_P (i.e., thermally lumped). The drag coefficient C_D and Nusselt number Nu_P in Eqs. (4) and (5) are expressed in terms of a particle Reynolds number Re_P $(= D_P\rho_g|\boldsymbol{u}_P - \boldsymbol{u}_g|/\mu_g)$, using the following standard drag and heat-transfer correlations for a sphere.

$$C_D = \begin{cases} 24\left(1 + Re_P^{\frac{2}{3}}/6\right)/Re_P & \text{for} \quad Re_P \le 1000 \\ 0.424 & \text{for} \quad Re_P > 1000 \end{cases} \quad (6)$$

$$Nu_P = 2\left[1 + Re_P^{\frac{1}{2}}Pr_g^{\frac{1}{3}}/3\right] \quad (7)$$

Table 1 Thermo-physical particle and gas properties

Property	Value
$C_l = C_s = C_P$	1046 J/kg-K
h_{lg} (evaporation)	11,834.82 kJ/kg
h_{ls} (melting)	396 kJ/kg
$h_{r,ls}$ (heterogeneous surface reactions)	−31,000 kJ/kg
$h_{r,gs}$ (homogeneous gas-phase reactions)	−43,334.82 kJ/kg
$Pr_g = Sc_g$	0.613
$T_{M,Al}$	934 K
ν_{ox}	0.886
$\rho_l = \rho_s = \rho_P$	2700 kg/m^3
E_a	95,395 J/mol
A_1	200 kg/m^2
$Y_{ox,\infty}$	0.233

B. Stage II—Quasi-Steady Combustion

1. Gas-Phase Analysis

After the particle heats up to T_{trans}, reactions are assumed to shift from the surface to the vapor phase. The vapor-phase combustion is then treated using an extension of the conserved scalar formulations for hydrocarbon droplets.[24] In this approach, standard approximations that readily allow for a semi-analytical solution are employed. These approximations include a unity Lewis number, ρD_m is a constant (i.e., Chapman gas assumption) and constant specific heats. Therefore the steady-state, one-dimensional spherical, transport equations are the same as classical hydrocarbon droplet analysis except that the total mass flux is interpreted to be the sum of fluxes caused by gas plus metal oxide. The exact phase of the metal oxide (i.e., solid vs gas) is not delineated because it is assumed that the diffusion of the small metal-oxide particles in its fume is the same as that of the gaseous species. This appears to be reasonable because the products of combustion include gaseous suboxide species such as AlO, AlO_2, and Al_2O, which are thought to condense out while forming Al_2O_3 as they diffuse from the flame to the particle surface. In addition, effects of thermophoretic diffusion also push the metal-oxide particles from the hot flame to the cooler surface. The current approximation might therefore account for the leading-order effect of thermophoretic diffusion because the temperature and species gradients are proportional to each other. The novelty of the current analysis is the inclusion of oxide deposition on the particle surface through the surface boundary conditions. A surface sink term $\dot{S}''_{mox}$ is introduced to account for the deposition of metal oxide. This results in a modification of the usual Shavb–Zeldovich coupling functions.[24,25] The boundary conditions with deposition present become as follows:

Total mass:

$$\dot{m}''_l - \dot{S}''_{mox} = \dot{m}''_{T,slg} \quad (8)$$

Metal mass:

$$\dot{m}''_l = \dot{m}''_{m,slg} = Y_m\dot{m}''_{T,slg} - \rho D_m\left.\frac{dY_m}{dr}\right|_{slg} \quad (9)$$

Oxidizer mass:

$$0 = \dot{m}''_{ox,slg} = Y_{ox,slg}\dot{m}''_{T,slg} - \rho D_m\left.\frac{dY_{ox}}{dr}\right|_{slg} \quad (10)$$

Metal-oxide mass:

$$-\dot{S}''_{mox} = \dot{m}''_{mox,slg} = Y_{mox,slg}\dot{m}''_{T,slg} - \rho D_m\left.\frac{dY_{mox}}{dr}\right|_{slg} \quad (11)$$

Product gas mass:

$$0 = \dot{m}''_{p,slg} = Y_{p,slg}\dot{m}''_{T,slg} - \rho D_m\left.\frac{dY_p}{dr}\right|_{slg} \quad (12)$$

Inert mass:

$$0 = \dot{m}''_{I,slg} = Y_{I,slg}\dot{m}''_{T,slg} - \rho D_m\left.\frac{dY_I}{dr}\right|_{slg} \quad (13)$$

Energy:

$$\begin{aligned} \dot{q}''_c|_l + \dot{m}''_l h_l - \dot{S}''_{mox}h_{mox} &= \dot{q}''_{rad}|_{slg} + \dot{m}''_{T,slg}h_{slg} - \rho D_m\left.\frac{dh}{dr}\right|_{slg} \\ &= \dot{q}''_c|_{slg} + \dot{q}''_{rad}|_{slg} + \sum_i \dot{m}''_i h_i|_{slg} \end{aligned} \quad (14)$$

For the burning of aluminum in air, the inert species is N_2. The only additional product gases are those that form metal oxide. However, the inclusion of product gases is left in the analysis so it could also be applied to a more general oxidizing environment (e.g., combustion

of aluminum in water vapor producing hydrogen gas). The assumption of constant specific heats allows the energy boundary condition, Eq. (14), to be written as follows:

Energy:

$$\dot{q}_c''|_l = \dot{q}_{\rm rad}''|_{\rm slg} + \dot{q}_c''|_{\rm slg} + \dot{m}_l'' h_{\rm lg} \tag{15}$$

where the $\dot{S}_{\rm mox}''$ sink term has been cancelled with the metal-oxide contribution in the enthalpy summation in Eq. (14) via Eq. (11).

Similar to a hydrocarbon droplet analysis, a conserved scalar approach is used to solve the transport equations along with their corresponding jump conditions resulting in the following set of coupling functions b (following the same notation of Kuo[25]),

$$b_{\rm m\text{–}ox} = \frac{Y_m - Y_{\rm ox}/\nu_{\rm ox}}{Y_{\rm m,slg} - (Y_{\rm ox,slg}/\nu_{\rm ox} + f + 1)}$$

$$b_{\rm m\text{–}mox} = \frac{Y_m - Y_{\rm mox}/\nu_{\rm mox}}{Y_{\rm m,slg} - [Y_{\rm mox,slg}/\nu_{\rm mox} + (1 + 1/\nu_{\rm mox})f + 1]}$$

$$b_{m\text{–p}} = \frac{Y_m - Y_p/\nu_p}{Y_{\rm m,slg} - (Y_{\rm p,slg}/\nu_p + f + 1)}, \qquad b_I = \frac{Y_I}{Y_{\rm I,slg}}$$

$$b_{m\text{–T}} = \frac{C_T T - Y_m h_{\rm r,gs}}{h_{\rm lg}' + h_{\rm r,gs}(f + 1 - Y_{\rm m,slg})} \tag{16}$$

where the fraction f is defined as the ratio of $\dot{S}_{\rm mox}''$ to $\dot{m}_T''$ (i.e., $f = \dot{S}_{\rm mox}''/\dot{m}_T''$) and $h_{\rm lg}'$ is the effective latent heat of vaporization defined as $h_{\rm lg}' = h_{\rm lg}(f + 1) + (\dot{q}_{\rm rad}''|_{\rm slg} - \dot{q}_c''|_l)/\dot{m}_T''$. By construction, each of the functions in Eq. (16) has exactly the same analytical solution and is given as:

$$\dot{m}_T/(4\pi r) = \rho_{\rm slg} D_m \ell n\{(b_\infty - b_{\rm slg} + 1)/[b(r) - b_{\rm slg} + 1]\} \tag{17}$$

Evaluating these functions at the surface of the liquid then results in a coupled set of nonlinear algebraic relations given as $\dot{m}_T/(4\pi r_{\rm slg}) = \rho_{\rm slg} D_m \ell n[1 + b_\infty - b_{\rm slg}] = \rho_{\rm slg} D_m \ell n[1 + B]$, where B is the transfer number defined as $B = b_\infty - b_{\rm slg}$. The total number of independent equations is equal to $n_p + n_I + 3$, where n_p and n_I are the number of product gaseous species and inerts, respectively. The expression relating $\dot{m}_T''$ to B is omitted from this count because only B, not $\dot{m}_T''$, is included as an unknown. Assuming a liquid–vapor equilibrium, a Clausius–Clapeyron relation can be introduced to relate the metal vapor pressure to the local surface temperature bringing the total number of equations to $4 + n_p + n_I$. The total number of unknowns equals $2(n_p + n_I + 4) + 3$ that includes unknown values of the mass fraction of all species and temperature at the surface of the particle and at the far field, as well as values for B, $\dot{S}_{\rm mox}''$ (or f) and $\dot{q}_c''|_l$. Note, radiation ($\dot{q}_{\rm rad}''|_{\rm slg}$) is omitted in this count, but can easily be included because the expression for radiation is given in terms of local surface properties. Assuming that the far-field values can be specified for all quantities reduces the total number of unknowns to $n_p + n_I + 7$. Subtracting the number of equations from the number of unknowns results in the requirement that three additional constraints must be imposed to close the system. The first is the usual assumption that $Y_{\rm ox,slg} = 0$, which assumes no oxidizer diffuses through the flame. Note that the flame does not have to be infinitely thin to satisfy this requirement. The second constraint is that the heat flux into the particle is modeled as $\dot{q}_c''|_l \simeq -k_l(T_{\rm slg} - T_P)/r_P$, where T_P is the bulk temperature that is known by solving for the liquid phase using a lumped approximation (to be discussed). The use of this model occasionally results in unrealistically large values of heat flux. To prevent this a flux limiter is introduced (see Appendix). Future work will examine the limitations of this assumption with comparisons to more refined liquid phase analysis (e.g., see the excellent discussion of Sirignano on related details[26]). However, in the spirit of maintaining a simple, computationally efficient representation of particle heating, the current approximation for $\dot{q}_c''|_l$ is felt to be adequate. For hydrocarbon combustion models, the first two constraints are all that are required. However, with the introduction of the $\dot{S}_{\rm mox}''$ term, an additional constraint is needed. Several possibilities were explored. The first considered is assuming that a thin flame sheet exists because the actual structure of the flame up to now has not been explicitly defined. Setting $b_{\rm m\text{–}ox}$ equal to $b_{\rm m\text{–}mox}$ at the flame sheet allows an explicit expression for f to be obtained. However, solutions using this approach result in nonphysical values for f. After much deliberation, the source of the problem was determined to be the solution for b itself given in Eq. (17). The main problem is that the value of $b_{\rm m\text{–}mox}$ across the flame sheet is discontinuous when $\dot{S}_{\rm mox}'' \neq 0$; therefore, the solution given in Eq. (17) is no longer valid. As a possible fix, one can determine the solution for $b_{\rm m\text{–}mox}$ by including the discontinuity in slope at $r = r_f$, which introduces an additional term that accounts for the jump in b across the flame; however, pursuing such an approach then eliminates the advantage of using a conserved scalar approach in the first place. Alternatively, a local closure for $\dot{S}_{\rm mox}''$ at the particle surface is more desirable. Several possible approaches can be explored depending on what is assumed and/or known to be the dominating physics controlling the deposition of metal oxide particles to the surface. However, a limiting case can be identified for which the deposition of metal oxide is sufficiently fast that the mass fraction of it at the particle surface is zero, that is, $Y_{\rm mox,slg} = 0$. This assumption provides an upper limit on the amount of metal oxide that can be deposited onto the surface. The same assumption has previously been used by Law to close the eigenvalue system under a flame sheet approximation.[8] Several other processes have also been postulated for the deposition of metal oxide onto the particle surface (e.g., such as entrainment of metal-oxide particles into a recirculation zone on the leeward side of the particle[13]). Such mechanisms are not considered in the present study. After imposing the just-mentioned constraints, the transfer numbers B for each coupling function can then be determined along with an explicit expression for f:

$$B_{\rm m\text{–}ox} = \frac{Y_{\rm m,slg} + Y_{\rm ox,\infty}/\nu_{\rm ox}}{f + 1 - Y_{\rm m,slg}} \tag{18}$$

$$B_{\rm m\text{–}mox} = \frac{(Y_{\rm mox,slg} - Y_{\rm mox,\infty})/\nu_{\rm mox} - Y_{\rm m,slg}}{Y_{\rm m,slg} - [Y_{\rm mox,slg}/\nu_{\rm mox} + (1 + 1/\nu_{\rm mox})f + 1]} \tag{19}$$

$$B_{m\text{–p}} = \frac{(Y_{\rm p,slg} - Y_{p,\infty})/\nu_p - Y_{\rm m,slg}}{Y_{\rm m,slg} - (Y_{\rm p,slg}/\nu_p + f + 1)} \tag{20}$$

$$B_I = (Y_{I,\infty}/Y_{\rm I,slg}) - 1 \tag{21}$$

$$B_{m\text{–T}} = \frac{C_{\rm T,slg}(T_\infty - T_{\rm slg}) + Y_{\rm m,slg} h_{\rm r,gs}}{h_{\rm lg}' + h_{\rm r,gs}(f + 1 - Y_{\rm m,slg})} \tag{22}$$

$$f = -\frac{(1 - Y_{\rm m,slg})(Y_{\rm mox,\infty}/\nu_{\rm mox} - Y_{\rm ox,\infty}/\nu_{\rm ox})}{(Y_{\rm mox,\infty} - Y_{\rm m,slg})/\nu_{\rm mox} - (1 + 1/\nu_{\rm mox})Y_{\rm ox,\infty}/\nu_{\rm ox}} \tag{23}$$

Equations (18–23) along with a vapor pressure relation for aluminum {i.e., $T_{\rm slg} = B/[A - \log(P)] - C$, where constants A, B, and C can be found in the website: http://webbook.nist.gov} represent a system of nonlinear algebraic equations that are nontrivial to solve. Details describing a relatively simple and efficient method for solving these equations for an arbitrary number of product and inert species are summarized in the Appendix.

2. *Liquid Metal and Metal-Oxide Analysis*

The liquid-phase system in the quasi-steady-burning mode is derived considering a moving control volume surface that surrounds the particle as it evaporates and accumulates metal-oxide mass. The control volume lies just outside the surface of the liquid and metal oxide. The distribution of velocity, density, and composition is assumed uniform throughout the particle. The temperature distribution is allowed to vary to accommodate unsteady heating effects and is expressed in terms of a lumped temperature T_P. Details on this type of control volume analysis can be found in Appendix A of Ref. 27. The result of this analysis is compatible with the gas-phase treatment and leads to the following system of ordinary differential equations

(ODE) governing the evolution of particle properties with time:

$$\frac{\mathrm{d}m_P}{\mathrm{d}t} = -\pi D_l \frac{\mu_g}{Sc_g} B Sh_g = \dot{m}_P \tag{24}$$

$$\frac{\mathrm{d}m_l}{\mathrm{d}t} = (f+1)\dot{m}_P = \dot{m}_l \tag{25}$$

$$m_P C_P \frac{\mathrm{d}T_P}{\mathrm{d}t} = \pi D_l \frac{\mu_g C_{\mathrm{T,slg}}}{Pr_g} \Delta T Nu_P + \dot{m}_l h_{\mathrm{lg}} - \dot{q}''_{\mathrm{rad}}|_{\mathrm{slg}} A_P \tag{26}$$

$$m_P \frac{\mathrm{d}\boldsymbol{u}_P}{\mathrm{d}t} = \frac{\pi}{8}\rho_g D_P^2 C_D |\boldsymbol{u}_g - \boldsymbol{u}_P|(\boldsymbol{u}_g - \boldsymbol{u}_P) + m_P \boldsymbol{g} \tag{27}$$

The subscripts l and P denote liquid and total mass weighted (i.e., liquid plus metal oxide) properties. The quantities D_l and D_P are the effective liquid diameter and total particle diameter respectively and are defined as $D_l = [6m_l/(\rho_l \pi)]^{1/3}$ and $D_P = \{6[m_l/\rho_l + (m_P - m_l)/\rho_{\mathrm{mox}}]/\pi\}^{1/3}$. The conservation equations are expressed in terms of effective Nusselt Nu_P and Sherwood Sh_P numbers so that simple corrections can be easily included to account for convective flow effects. In this study, Ranz–Marshall correlations[26,28] are used, that is, $Nu_P(Sh_P) = 2\{1 + Re_P^{1/2}[Pr_g(Sc_g)]^{1/3}/3\}\, \ell_n(1+B)/B$. The effective temperature difference ΔT given in Eq. (26) that is compatible with the gas-phase analysis is given as $\Delta T = T_\infty - T_{\mathrm{slg}} - h_{\mathrm{r,gs}}[B(f+1) - Y_{\mathrm{m,slg}}(1+B)]/C_{\mathrm{T,slg}}$. The drag correlation in Eq. (27) is the same as used in Eq. (4). Note, in the limit as $Re_P \to 0$ the Eqs. (24–26) reduce to the following:

$$\frac{\mathrm{d}m_P}{\mathrm{d}t} = = -\dot{m}''_T A_P \tag{28}$$

$$\frac{\mathrm{d}m_l}{\mathrm{d}t} = = -\dot{m}''_l A_P \tag{29}$$

$$m_P C_P \frac{\mathrm{d}T_P}{\mathrm{d}t} = -\dot{q}''_c|_l A_P \tag{30}$$

which is consistent with the gas-phase analysis.

The current formulation for stage II combustion can be easily extended beyond air oxidizing environments to include simultaneous multiple oxidizer environments. This extension simply requires the definition of additional coupling functions between the metal and all possible oxidizers (i.e., $b_{\mathrm{m-ox}_1}, b_{\mathrm{m-ox}_2}, b_{\mathrm{m-ox}_3} \ldots b_{\mathrm{m-ox}_n}$) requiring the replication of the oxidizer jump condition of Eq. (10) resulting in a relation $B_{\mathrm{m-ox}_i}$ for every possible oxidizer. To close the system, two additional constraints are required, assuming that the same model for conduction into the particle is used. One possibility is to again assume $Y_{\mathrm{mox}} = 0$ at the surface and also set the mass fraction of the most reactive oxidizer to zero at the surface. Another possibility is to set two of the oxidizers mass fractions to zero at the surface. Other extensions of the current model include the possibility of including HSR during the vapor-phase combustion. Nitrogen containing species such as NO_x and N_2 have been postulated to react with the aluminum metal at the particle surface forming aluminum nitride (AlN).[4,6] These effects could also be incorporated in the current model by the addition of a coupling function between the metal vapor and the nitrogen containing species (N), $b_{m-\mathrm{N}}$, with an appropriate boundary condition for the N species that includes its consumption rate $\dot{S}''_N$.

III. Numerical Implementation

The particle transport equations for stage I ignition and stage II combustion constitute a system of stiff ODE[5] that are integrated in time using the Lawrence Livermore Solver for Ordinary Differential Equations library.[29] All mixture weighted thermodynamic properties in Eqs. (1–5) and (24–27) are evaluated using standard polynomial fits taken from the CHEMKIN library[30] and available on the NIST webbook.[§]

[§]Data available online at http://webbook.nist.gov.

IV. Results and Discussion

The flow condition considered for assessing the utility of the current model is the case of a particle starting from rest and falling under the influence of gravity after being ignited. This configuration is common to many experimental studies for determining the overall burn rate and flame structure.[2–4,6,31,32] Specifically, burn rates and particle velocity are compared to the experimental measurements of Dreizin.[3] Four values of $T_{g,\infty}$ are considered corresponding to 1000, 1500, 2000, and 3000 K. Although the effects of radiation are included in model formulation, these effects are neglected. Brooks and Beckstead examined the sensitivity of radiation on the overall particle burn rate and concluded that for larger particles (i.e., $D_P > 50$–$100\ \mu$m), the heat radiated from the flame to the particle surface is small and only contributes to a 20% decrease in the overall burning time and even less for smaller particles.[10]

Figures 3–7 summarize the particle time-history properties for the cases under consideration. The initial particle diameter of 165 μm is chosen to match the experiments of Dreizin.[3] In the experiments the particles are ignited using a microarc device that superheats the particle to the boiling temperature of aluminum and also rapidly accelerates the particle to a speed of approximately 2 m/s (see Fig. 6

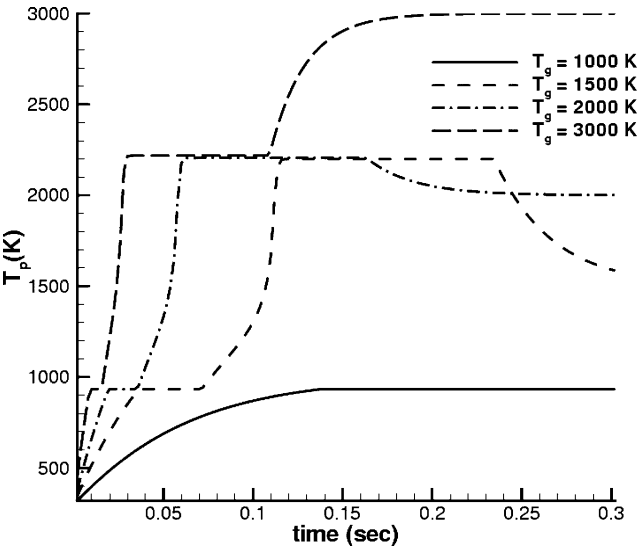

Fig. 3 Particle temperature time history for a 165-μm free-falling particle.

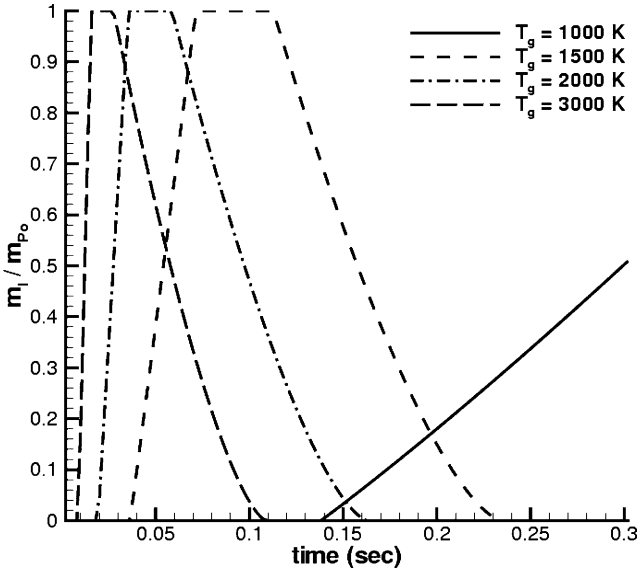

Fig. 4 Normalized liquid mass time history for a 165-μm free-falling particle.

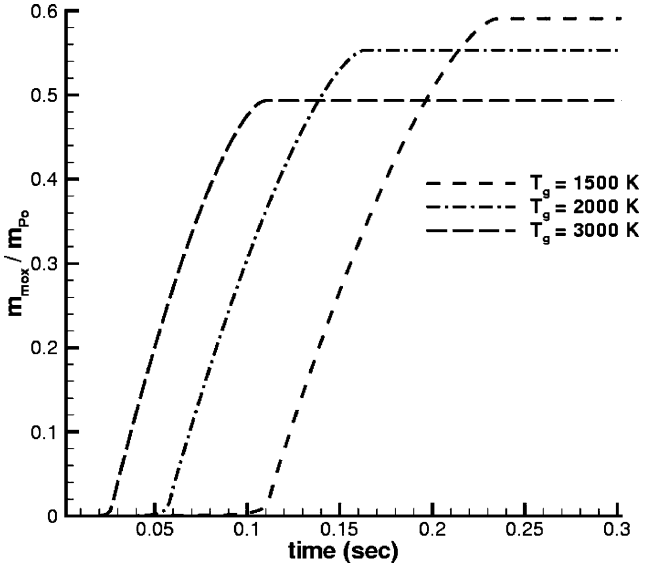

Fig. 5 Normalized metal-oxide mass time history for a 165-μm free-falling particle.

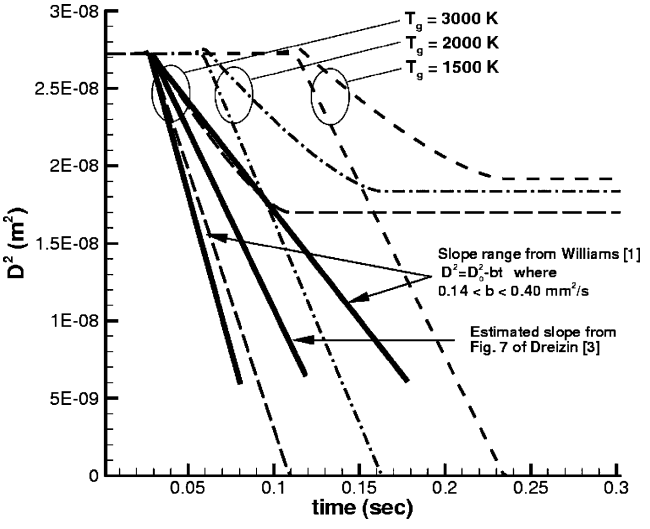

Fig. 6 Diameter time history for a 165-μm free-falling particle using the liquid diameter and total diameter (liquid + metal oxide) with experimental correlation from Williams,[1] $D^2 = D_o^2 - bt$, for the limits of $b = 0.14$ and 0.40 mm^2/s and $b = 0.23$ mm^2/s that is estimated from Fig. 7 of Dreizin.[3]

of Ref. 3). In the current numerical results, the initial temperature of the particle is set to 300 K and the velocity set equal to zero, therefore, direct comparisons to data are only made for the vapor-phase burning stages.

Figure 3 shows the particle temperature histories. For all of the temperature cases, the particle is observed to initially heat up to its melting temperature of $T_P = T_{\mathrm{M,Al}} = 934$ K and remain constant until melting is complete. For the higher temperature cases of $T_g = 1500$ K and above, ignition occurs followed by a quasi-steady burning and finally either cooling or heating of the remaining metal oxide to the surrounding gas temperature. As discussed in the model formulation, the transition from ignition to stage I ignition to stage II combustion is assumed to be a function of a transition temperature that is chosen arbitrarily to be $T_{\mathrm{trans}} = 2000$ K. Higher and lower values of 2100 and 1900 K are also explored resulting in very little difference in overall particle temperature history (not shown). This suggests that as long as the effects of HSR are accounted for in the model that the overall particle temperature history might not be too sensitive to the exact value of transition temperature, for the cases considered, because the time associated with

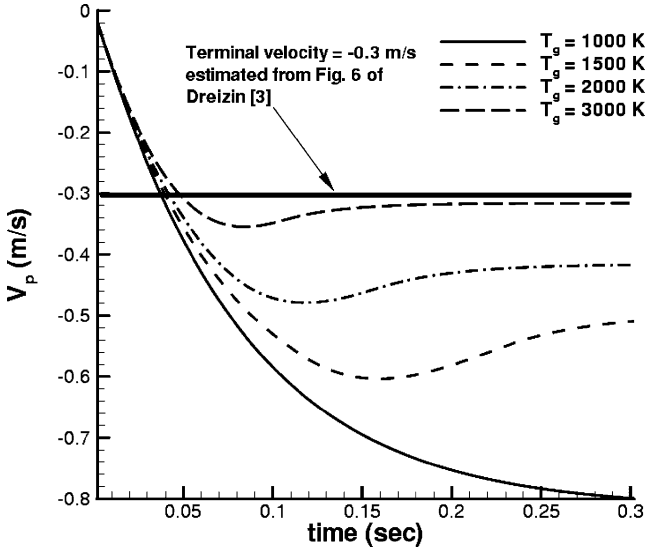

Fig. 7 Velocity time history for a 165-μm free-falling particle: ——, measured terminal velocity of −0.3 m/s taken from Fig. 6 of Dreizin.[3]

HSR is much smaller than any of the other processes. Also, neglecting the effects of HSR would result in ignition for cases only for which $T_g > T_{\mathrm{trans}}$, whereas the current model predicts ignition for a surrounding temperature between 1000 and 1500, but is generally a function of the phenomenological description of the surface reaction processes.

During the quasi-steady burning stage of the particle, the temperature of the particle remains constant when the convective heating exactly balances the energy loss from evaporation. For the 1-atm pressure considered, this temperature is 2206 K and is fairly insensitive to the surrounding gas temperature. This temperature is also slightly below the boiling temperature of $T_{\mathrm{b,Al}} = 2326.2$ K (for the vapor pressure curve used[¶]), consistent with the experimental findings of Bucher et al.[2]

Figure 4 shows the time histories of normalized liquid mass in the particle m_l/m_{P_o}, defined as the liquid metal mass divided by the initial particle mass. For $T_{g,\infty} \geq 1500$ K, m_l/m_{P_o} goes from zero to unity during the first 10 to 20 ms as the particle melts, corresponding to the constant temperature region shown in Fig. 3. For the $T_g = 1000$ K case, the particle is approximately 50% melted after 300 ms.

Figure 5 shows the time history of metal oxide mass m_{mox} on the particle normalized by the initial particle mass m_{P_o}. Final values of m_{mox}/m_{P_o} range from approximately 50% at higher temperatures to nearly 60% for the lower-temperature cases. These values represent the maximum amount of oxide caps formed, within the scope of the current analysis, and are consistent with previous theoretical studies using a variant of Law's model.[9]

Figure 6 shows the time history of D^2. For each temperature case, D^2 lines are plotted based on the liquid mass D_{s+l} and the total mass D_P, the difference between these being the contribution from the metal oxide. As shown, D_P first increases slightly just before the quasi-steady burning, corresponding to the added metal-oxide mass from HSR, then decreases from evaporation mass loss, and finally attains a constant value because $m_{\mathrm{mox}} \gg m_l$. Also in Fig. 6 are experimentally derived D^2 correlations from Williams,[1] $D^2(t) = D_o^2 - bt$, with b ranging from 0.14 to 0.40 mm^2/s (solid lines) along with a case for $b = 0.24$ mm^2/s (solid line) that is estimated from the experimental curve fit from Fig. 7 of Dreizin[3] for the mean slope. For all cases, the slope of the predicted D_{l+s}^2 lies within the range of reported values and, within experimental scatter, agrees well with the experiment of Dreizin. As expected, the magnitude of the slope based on D_P is less. The slope based on D_P also agrees well to the lower bound of $b = 0.14$, suggesting that perhaps the experimental

[¶]Data available online at http://webbook.nist.gov.

scatter in reported particle sizes might be in part caused by simply identifying the particle liquid-phase diameter from high-speed images.

As stated earlier, the current formulation does not required any explicit assumption on the thickness of the flame structure surrounding the particle. However, if the flame is assumed to be infinitely thin then an estimate the flame radius can be determined using the $b_{\text{m–ox}}$ coupling function and assuming $Y_m = Y_{\text{ox}} = 0$ at $r = r_f$ resulting in the following expression for flame radius:

$$r_f = \left\{ \frac{-4\pi\mu_g}{Sc_g\,\dot{m}_P}\,\ell_n\left[\frac{Y_{\text{ox},\infty}/\nu_{\text{ox}} + f + 1}{f+1}\right]\right\}^{-1} \tag{31}$$

Using Eq. (31), r_f/r_l is calculated to be equal to 3.01, 3.14, and 3.39 for $T_g = 1500$, 2000, and 3000 K, respectively, and are slightly larger than the range reported by Dreizin of $2.42 < r_f/r_l < 3.03$ (Ref. 3).

Figure 7 shows the time history of particle velocity. For the particles that ignited, the velocity initially increases as the particle accelerates from gravity, then decreases as the particle reduces in size from burning, and finally reaches a constant value associated with the terminal velocity of the residual oxide cap mass. The higher the surrounding temperature, the lower is the residual oxide mass (see Fig. 5), resulting in lower terminal velocities as shown in Fig. 7. The magnitude of the terminal velocity for the $T_g = 3000$ K case is 0.32 m/s and matches remarkably well to the experimentally measured terminal velocity of $\simeq$0.3 m/s from Dreizin.[3]

V. Conclusions

In this study a mechanistic model for aluminum particle ignition and combustion in air is developed. The model consists of two stages, a stage I ignition event and a stage II quasi-steady combustion. A new conserved scalar formulation is presented, which includes the effects of metal-oxide deposition on the surface of the particle that does not rely on standard flame sheet assumptions. Results using this model for the ignition of free-falling particles show good agreement to experimental measurements of overall burn rates, flame radius, and terminal velocity.

Appendix: Solution of Gas-Phase System

Equations (18–23) along with a vapor pressure curve for the metal vapor comprise a system of nonlinear algebraic equations. The procedure for finding the roots for this system of equations starts with an initial guess for the mass fraction of the metal vapor at the surface of the particle $Y^{guess}_{\text{m,slg}}$. The equations are arranged in an order so as to obtain a new value of $Y^{new}_{\text{m,slg}}$ using the following steps:

1) Guess an initial value of $Y_{\text{m,slg}}$ using expression given next.

2) Determine, f, where $f = -[(1 - Y_{\text{m,slg}})\,(Y_{\text{mox},\infty}/\nu_{\text{mox}} - Y_{\text{ox},\infty}/\nu_{\text{ox}})]/[(Y_{\text{mox},\infty} - Y_{\text{m,slg}})/\nu_{\text{mox}} - (1 + 1/\nu_{\text{mox}})Y_{\text{ox},\infty}/\nu_{\text{ox}}]$.

3) Determine B using $B_{\text{m–ox}} = (Y_{\text{m,slg}} + Y_{\text{ox},\infty}/\nu_{\text{ox}})/(1 - Y_{\text{m,slg}} + f)$.

4) Determine $\dot{m}''_T = 2\mu_\infty\,\ell_n(1 + B)/(Sc_g D_P)$.

5) Determine composition at surface using $Y_{\text{i,slg}} = \nu_i Y_{\text{m,slg}} + [Y_{i,\infty} - \nu_i(f + 1)B]/(1 + B)$, where ν_I and ν_{ox} are >0, $\nu_p < 0$, and $\nu_I = 0$ and determine the sum (Σ_{Y_i}), which might not equal 1.

6) Renormalize species so that their sum plus $Y_{\text{m,slg}}$ equals 1, $Y_{\text{i,slg}} = Y_{\text{i,slg}}(1 - Y_{\text{m,slg}})/(\Sigma_{Y_i} - Y_{\text{m,slg}})$.

7) Determine $MW_{\text{mix,slg}} = (\sum Y_{\text{i,slg}}/MW_i)^{-1}$.

8) Determine the vapor pressure $P_{\text{m,vap}} = Y_{\text{m,slg}} P MW_{\text{mix}}/MW_m$.

9) Determine T_{slg} from Clausius–Clapeyron relation.

10) Mixture $C_{\text{T,slg}}$ determined using $Y_{\text{i,slg}}(T)$ using standard polynomial curve fits for vapor species.[30,**]

11) Determine $\dot{q}''_c|_l = -q_{\text{limiter}} k_l\,(T_{\text{slg}} - T_P)/r_P$, where $q_{\text{limiter}} = MIN[|h_{\text{lg}}\dot{m}''_T(f + 1)|/|k_l(T_{\text{slg}} - T_P)/r_P|, 1]$.

12) Determine new value of B using $B_{m\text{–T}}$, that is, $B^{new} = [C_{\text{T,slg}}(T_\infty - T_{\text{slg}}) + Y_{\text{m,slg}}h_{\text{r,gs}}]/[h'_{\text{lg}} - h_{\text{r,gs}}(Y_{\text{m,slg}} - 1 - f)]$, where $h'_{\text{lg}} = h_{\text{lg}}(f + 1) + (\dot{q}''_{\text{rad}}|_{\text{slg}} - \dot{q}''_c|_l)/\dot{m}''_T$.

**Data available online at http://webbook.nist.gov.

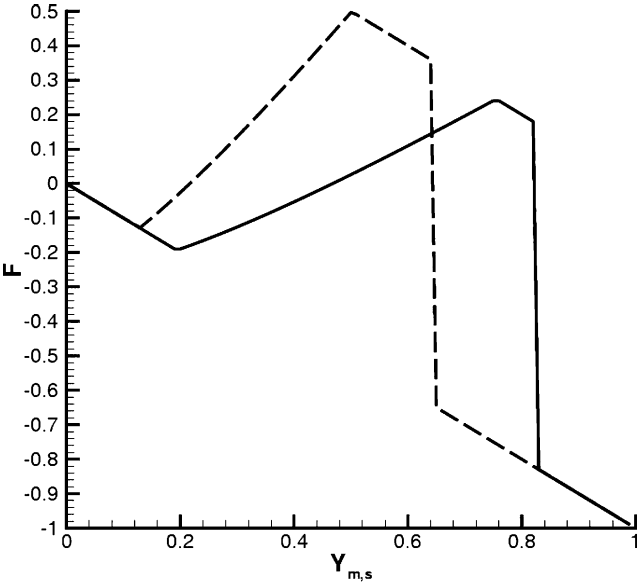

Fig. A1 Plots of function F vs $Y_{\text{m,slg}}$ assuming $\dot{q}''_c|_l = 0$ (——) and with conduction $\dot{q}''_c|_l = -q_{\text{limiter}} k_l\,(T_{\text{slg}} - T_P)/r_P$ (– – –) for $T_g = T_P = 2000$ K.

13) Recalculate $Y_{\text{m,slg}}$ using $B_{\text{m–ox}}$ relation, $Y^{new}_{\text{m,slg}} = [(f + 1)B^{new} - Y_{\text{ox},\infty}/\nu_{\text{ox}}]/(1 + B^{new})$.

A function $F = Y^{new}_{\text{m,slg}} - Y^{guess}_{\text{m,slg}}$ is defined for the root of this function then corresponds to the solution of nonlinear algebraic equations. Figure A1 shows a typical result of F as a function of $Y^{guess}_{\text{m,slg}}$ assuming $\dot{q}''_c|_l = 0$ (solid line) and $\dot{q}''_c|_l = -q_{\text{limiter}} k_l\,(T_{\text{slg}} - T_P)/r_P$. As shown, there are two roots. The right most root is nonphysical. An estimate of the root location location is determined by assuming $f = 0$ and $\dot{q}''_c|_l = 0$. With these assumptions then an initial guess for $Y_{\text{m,slg}}$ is obtained by equating $B_{m\text{–T}}$ to $B_{\text{m–ox}}$, resulting in the following result:

$$Y^{guess}_{\text{m,slg}} = \frac{C_{\text{T,slg}}(T_\infty - T_{\text{slg}}) - Y_{\text{ox},\infty}(h_{\text{r,gs}} + h_{\text{lg}})/\nu_{\text{ox}}}{C_{\text{T,slg}}(T_\infty - T_{\text{slg}}) + h_{\text{lg}} - h_{\text{r,gs}}Y_{\text{ox},\infty}/\nu_{\text{ox}}} \tag{A1}$$

This estimate is first used in a Newton–Raphson method to locate the root of F that converges quickly, typically within six iterations. Occasionally this method fails, and a bisectional algorithm is used as a backup with the initial upper and lower bounds of the region set equal to $Y^{guess}_{\text{m,slg}} \pm 0.2$, respectively. The bisectional algorithm always located a root but with additional cost requiring 30–40 iterations to satisfy an error tolerance of 1×10^{-10}.

Acknowledgments

This work is supported by the Defense Threat Reduction Agency and Sandia National Laboratories under Contract 64782 with John Kolts, Mel Baer, and Gene Hertel serving as technical monitors.

References

[1]Williams, F. A., "Some Aspects of Metal Particle Combustion," *Physical and Chemical Aspects of Combustion*, edited by F. L. Dryer and R. F. Sawyer, Gordon and Breach Science Publ., Amsterdam, The Netherlands, 1997, pp. 267–288.

[2]Bucher, P., Yetter, R. A., Dryer, F. L., Parr, T. P., Hanson-Parr, D. M., and Vicenzi, E. P., "Flame Structure Measurement of Single, Isolated Aluminum Particles Burning in Air," *Proceedings of 26th Symposium (International) on Combustion*, The Combustion Inst., Pittsburgh, PA, 1996, pp. 1899–1908.

[3]Dreizin, E. L., "Experimental Study of Stages in Aluminum Particle Combustion in Air," *Combustion and Flame*, Vol. 105, No. 4, 1996, pp. 541–556.

[4]Dreizin, E. L., "On the Mechanism of Asymmetric Aluminum Particle Combustion," *Combustion and Flame*, Vol. 117, No. 4, 1999, pp. 841–850.

[5]Dreizin, E. L., "Phase Changes in Metal Combustion," *Progress in Energy and Combustion Science*, Vol. 25, No. 1, 2000, pp. 57–78.

[6]Bucher, P., Yetter, R. A., Dryer, F. L., Vicenzi, E. P., Parr, T. P., and Hanson-Parr, D. M., "Condensed-Phase Species Distributions About Al Particles Reacting in Various Oxidizers," *Combustion and Flame*, Vol. 117, Nos. 1–2, 1999, pp. 351–361.

[7]Brzustowski, T. A., and Glassman, I., "Vapor-Phase Diffusion Flames in the Combustion of Magnesium and Aluminum. I: Analytical Developments," *Heterogeneous Combustion*, edited by H. G. Wolfhard, Progress in Astronautics and Aeronautics, Vol. 15, Academic Press, New York, 1964, pp. 75–116.

[8]Law, C. K., "A Simplified Theoretical Model for the Vapor-Phase Combustion of Metal Particles," *Combustion Science and Technology*, Vol. 7, 1973, pp. 197–212.

[9]Turns, S. R., Wong, S. C., and Ryba, E., "Combustion of Aluminum-Based Slurry Agglomerates," *Combustion Science and Technology*, Vol. 54, 1987, pp. 299–318.

[10]Brooks, K. P., and Beckstead, M. W., "Dynamics of Aluminum Combustion of Metal Particles," *Journal of Propulsion and Power*, Vol. 11, No. 4, 1995, pp. 769–780.

[11]Liang, Y., and Beckstead, M. W., "Numerical Simulation of Unsteady, Single Aluminum Particle Combustion in Air," AIAA Paper 98-3825, 1998.

[12]Widener, J. F., Liang, Y., and Beckstead, M. W., "Aluminum Combustion Modeling in Solid Propellant Environments," AIAA Paper 99-2629, 1999.

[13]Babuk, V. A., and Vasilyev, V. A., "Model of Aluminum Agglomerate Evolution in Combustion Products of Solid Rocket Propellant," *Journal of Propulsion and Power*, Vol. 18, No. 4, 2002, pp. 814–823.

[14]Atkinson, A., "Transport Processes During the Growth of Oxide Film at Elevated Temperature," *Reviews of Modern Physics*, Vol. 57, No. 2, 1985, pp. 437–470.

[15]Schütze, M., "Fundamentals of High Temperature Corrosion," *Materials Science and Technology*, edited by R. W. and Haasen P. Cahn and E. J. Kramer, Wiley-VCH, New York, 2000, pp. 68–128.

[16]Rode, H., Hlavacek, V., Viljoen, H. J., and Gatica, J. E., "Combustion of Metallic Powders: A Phenomenological Model for the Initiation of Combustion," *Combustion Science and Technology*, Vol. 88, Nos. 3–4, 1993, pp. 153–175.

[17]Jeurgens, L. P. H., Sloof, W. G., Tichelaar, F. D., and Mittermeijer, E. J., "Growth Kinetics and Mechanics of Aluminum-Oxide Films Formed by Thermal Oxidation of Aluminum," *Journal of Applied Physics*, Vol. 92, No. 3, 2002, pp. 1649–1656.

[18]Kuehl, D. K., "Ignition and Combustion of Aluminum and Beryllium," *AIAA Journal*, Vol. 3, No. 12, 1965, pp. 2239–2247.

[19]Wong, S. C., and Turns, S. R., "Ignition of Aluminum Slurry Droplets," *Combustion Science and Technology*, Vol. 52, 1987, pp. 50–55.

[20]Servaites, J., Krier, H., Melcher, J. C., and Burton, R. L., "Ignition and Combustion of Aluminum Particles in Shocked H_2O/O_2/Ar and CO_2/O_2/Ar Mixtures," *Combustion and Flame*, Vol. 125, Nos. 1–2, 2001, pp. 1040–1054.

[21]Widener, J. F., "Computer Modeling of Aluminum Particle Heat-up and Combustion Under Rocket Motor Conditions," M.S. Thesis, Dept. of Chemical Engineering, Brigham Young Univ., UT, 1998.

[22]Foelsche, R. O., Burton, R. L., and Krier, H., "Ignition and Combustion of Aluminum Particles in $H_2O/O_2/N_2$ Products," *Journal of Propulsion and Power*, Vol. 14, No. 6, 1998, pp. 1001–1008.

[23]Roberts, T. A., Burton, R. L., and Krier, H., "Ignition and Combustion of Aluminum/Magnesium Alloy Particles in O_2 at High Pressures," *Combustion and Flame*, Vol. 92, Nos. 1–2, 1993, pp. 125–143.

[24]Glassman, I., *Combustion*, 3rd ed., Academic Press, New York, 1996, pp. 298–312.

[25]Kuo, K. K., *Principles of Combustion*, Wiley-Interscience, New York, 1986, pp. 380–385.

[26]Sirignano, W. A., *Fluid Dynamics and Transport of Droplets and Sprays*, Cambridge Univ. Press, Cambridge, England, U.K., 1999, Chaps. 2 and 3.

[27]Crowe, C., Sommerfeld, M., and Tsuji, Y., *Multiphase Flows with Droplets and Particles*, CRC Press, New York, Appendix A, 1998.

[28]Ranz, W. E., and Marshall, W. R., "Evaporation from Drops," *Chemical Engineering Progress*, Vol. 48, No. 3, 1952, pp. 141–173.

[29]Radhakrishnan, K., and Hindmarsh, A. C., "Description and Use of LSODE, the Livermore Solver for Ordinary Differential Equations," Lawrence Livermore National Lab., Technical Report UCRL-ID-113855, Livermore, CA, Dec. 1993.

[30]Kee, R. J., Rupley, F. M., and Miller, J. A., "The CHEMKIN Thermodynamic Data Base," Sandia National Lab., Technical Report SAND87-8215, Livermore, CA, April 1987.

[31]Dreizin, E. L., "Experimental Study of Aluminum Particle Flame Evolution in Normal and Micro-Gravity," *Combustion and Flame*, Vol. 116, No. 3, 1999, pp. 324–333.

[32]Olsen, S. E., and Beckstead, M. W., "Burn Time Measurements of Single Aluminum Particles in Stream and CO_2 Mixtures," *Journal of Propulsion and Power*, Vol. 12, No. 4, 1996, pp. 662–671.